ACS Catalysis

pubs.acs.org/acscatalysis
Research Article

Defect-Engineered MoS_2 Supported Transition Metal Clusters for Electrochemical Reactions

Rafael L. H. Freire, Henrique A. B. Fonseca, Pedro Ivo R. Moraes, Mauricio Mocelim, Marionir M. C. B. Neto, and Juarez L. F. Da Silva*

Cite This: ACS Catal. 2025, 15, 20036−20048
Read Online

ABSTRACT: Electrochemical reactions such as hydrogen and oxygen evolution, as well as carbon dioxide reduction, are central to renewable energy conversion and storage technologies. The development of efficient and earth-abundant catalysts remains crucial for improving these processes. In this study, we employed density functional theory calculations combined with the computational hydrogen electrode model to investigate the catalytic behavior of transition-metal (TM) tetramer clusters (Fe_4, Co_4, Ni_4, Cu_4) supported on pristine and defected (sulfur vacancies) MoS_2 monolayers. The results reveal distinct reactivity trends driven by both the metal identity and the presence of sulfur vacancies, as well as their synergistic effects on cluster stability and activity. Except for Ni_4, the TM_4 clusters preferentially anchor near sulfur vacancies, where most clusters maintain their compact tetrahedral geometries, although Cu_4 exhibits noticeable distortions when located away from the vacancy sites. In the hydrogen evolution reaction, Fe_4@MoS_2 near a sulfur vacancy exhibits the most favorable activity, highlighting the beneficial role of defect sites in stabilizing adsorbates and tuning electronic properties (synergistic effects). For the oxygen evolution reaction, overpotentials spread from 0.95 to 2.0 V, with Co_4@MoS_2 positioned close to a vacancy emerging as the most active configuration. Regarding CO_2 reduction, only limited activity is observed, primarily for Co_4 and Cu_4 clusters located away from vacancies; however, the competing hydrogen evolution and surface poisoning by OH intermediates significantly hinder selectivity. Overall, these findings establish clear activity trends across different reactions and emphasize the synergistic role of cluster composition and defect engineering in tailoring the catalytic landscape of non-noble-metal MoS_2-based electrocatalysts.

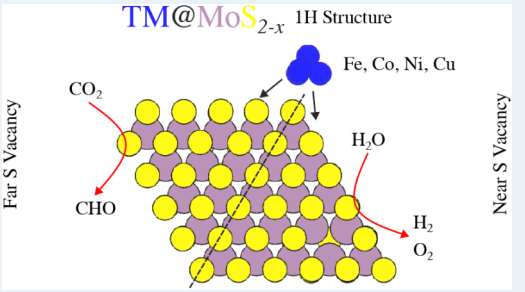

KEYWORDS: *hydrogen evolution reaction, oxygen evolution reaction, carbon dioxide reduction reaction, transition-metal dichalcogenides, computational simulations*

1. INTRODUCTION

Renewable energy sources, including solar and wind, have emerged as viable alternatives within the framework of a low-carbon economy.[1,2] However, their intermittent nature requires the development of efficient strategies for energy storage and conversion. Electrochemical processes, including the hydrogen evolution reaction (HER),[3,4] oxygen evolution reaction (OER),[5,6] and carbon dioxide reduction reaction (CO_2RR),[7,8] are critical components of these strategies. They offer promising pathways for the generation of sustainable fuels and the realization of carbon-neutral energy systems. Among these processes, HER and OER are vital for the splitting of water (H_2O) and the generation of molecular hydrogen (H_2), which is a high energy density and environmentally benign fuel, while CO_2RR offers a pathway for the conversion of greenhouse gases into value-added chemicals and fuels.[7−11] A significant challenge across the three reactions lies in the development of electrocatalysts that are efficient, stable, and cost-effective.[12,13] Notable advancements have been achieved with materials such as earth-abundant transition metals, including Fe and Ni,[3] transition-metal (TM) phosphides,[14] and TM dichalcogenides (TMDs).[15]

Two-dimensional (2D) TMDs, particularly MoS_2, can adopt distinct structures, namely trigonal prismatic (2H) or octahedral (1T).[16,17] The semiconducting 2H structure is more stable, whereas the metallic 1T structure is metastable.[18,19] The application of MoS_2 to HER has shown good results due to active edges and structural defects.[20−22] However, the lack of reactive basal planes and hydrophobic characteristics limits electrochemical applications.[23] Furthermore, MoS_2 has also been applied to OER, which makes this material a dual catalyst for H_2O splitting with performance comparable to IrO_2, which has been considered the state-of-the-art material for OER.[24]

Received: August 23, 2025
Revised: October 18, 2025
Accepted: November 5, 2025

https://doi.org/10.1021/acscatal.5c05963
ACS Catal. 2025, 15, 20036−20048

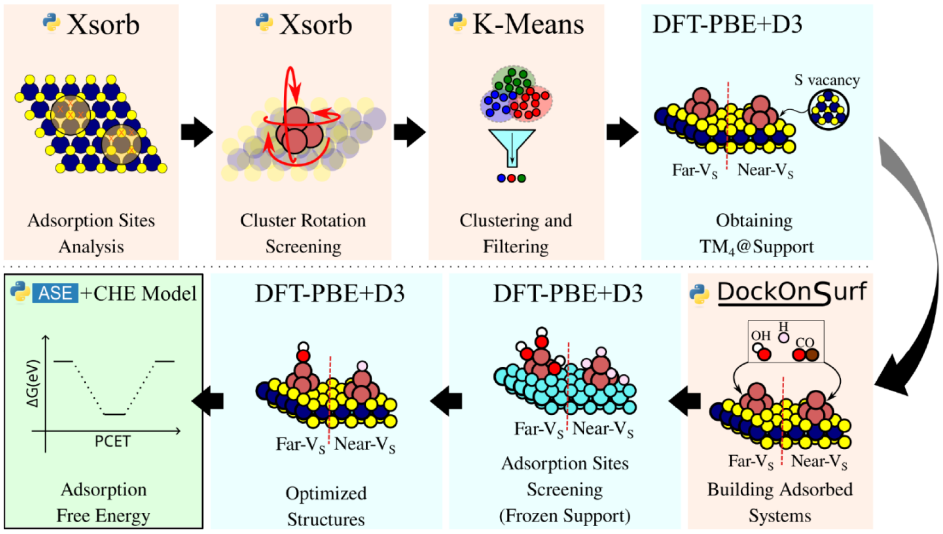

Figure 1. Schematic representation of the flowchart of the methodologies employed in this work. Procedures for constructing and selecting structures, mainly using Python packages like `Xsorb`[34] and `DockOnSurf`,[35] are indicated by a red background. Subsequent computational calculations based on DFT are shown in blue. The final properties obtained, such as the adsorbed Gibbs free energy of the electrochemical reaction steps studied, are presented in the green-colored region. "Python" and the Python logos are trademarks or registered trademarks of the Python Software Foundation, used by the authors with permission from the Foundation.

Different strategies have been used to improve MoS_2 efficiency for electrochemical reactions, e.g., the incorporation of S vacancies (V_S) usually improves the reactivity of basal planes, with free energies (ΔG_{H^*}) comparable to the compact Pt(111) surface.[25,26] For CO_2RR, another work showed that V_S play the major role in dissociating CO_2 into CO and O.[27] Electrocatalysts can benefit from the combination of different dimensionality materials; for example, the addition of single atoms or even small TM clusters on MoS_2 can lead to changes in the electronic structure, in which TM donates electrons and reduces the band gap of the material, which is advantageous for applications as electrodes.[28] However, studies based on the use of Co showed that the formation energy is large, indicative of low thermodynamic stability, which implies that there exist critical challenges between theoretical and practical applications.[29]

Despite these promising strategies, our understanding of the atomistic mechanisms that drive activity in multiple electrochemical reactions in clusters of TM supported on defective MoS_2 remains limited. Treating electrochemical reactions as independent processes can be misleading, as several reactions are inherently competitive. For example, HER and OER are competing half-cell reactions that occur at the same electrode−electrolyte interface,[30] while in CO_2RR, HER and OH desorption may compete with CO_2 reduction pathways.[8,31] In both cases, the combination of impurities or defects such as single atoms, TM clusters, and V_S adsorbed on the surface can synergistically modulate the local structural and electronic environment. Thus, it influences the kinetics, selectivity, and thermodynamics of all reactions involved.[8,25,32,33]

By simultaneously examining HER, OER, and CO_2RR within a unified theoretical framework, an improved understanding of dual or trifunctional electrocatalytic behavior could emerge in realistic defective materials. The combination of MoS_2, V_S, and TM_4 offers many possibilities to tune the properties and improve the reactivity of the catalyst. Furthermore, to our knowledge, V_S is an unexplored area, especially for the OER reaction. Taking into account these open problems, our objective is to investigate and improve our atomistic understanding of the HER, OER, and CO_2RR reactions through engineering TM_4 clusters supported on pristine and defective (V_S) MoS_2 monolayers, where TM = Fe, Co, Ni, Cu. Furthermore, our intention is to analyze how different combinations of defects and TM_4 favor the mentioned electrochemical reactions, including TM_4 near and far from V_S.

Our theoretical study elucidates the interaction between the geometric configuration of the TM_4 cluster, the vicinity of V_S, and the catalytic activity in the MoS_2 monolayers. We demonstrate that V_S generally enhances the adsorption stability of the TM_4 clusters, except for Ni_4, which exhibits a preference for pristine regions. Despite the overall structural preservation, certain systems, such as Cu_4, undergo significant distortions that affect the catalytic behavior. Our ΔG_{H^*} analysis indicates that multiple configurations achieve near-optimal metrics for the HER. The Fe_4@MoS_2 system near a V_S manifests the most advantageous HER activity. In case of OER, the minimum overpotential is observed with Co_4@MoS_2 near a sulfur vacancy, which indicates it as a promising candidate for OER catalysis. In addition, anticipated scaling relationships are observed between the OH* and OOH* intermediates, suggesting a broader applicability of these results to chalcogenide-based catalytic systems. In contrast, although certain clusters, such as Co_4 and Cu_4, far from the vacancy, show partial promise for CO_2RR, their selectivity is significantly inhibited by concurrent HER activity and poisoning OH.

2. THEORETICAL APPROACH AND COMPUTATIONAL DETAILS

This study aims to investigate the influence of small TM_4 clusters in conjunction with S vacancy defects on the 2D MoS_2 substrate in the context of electrochemical reactions, specifically HER, OER and CO_2RR. Our analysis includes the Fe_4, Co_4, Ni_4, and Cu_4 clusters, allowing exploration of the effects associated with the occupation of the *d*-states during the

https://doi.org/10.1021/acscatal.5c05963
ACS Catal. 2025, 15, 20036−20048

electrochemical processes mentioned before. In summary, we combined density functional theory (DFT) and Python packages such as Xsorb,[34] DockOnSurf,[35] and k-means algorithm to obtain a representative set of supported clusters and then adsorbed molecules. Later, we investigated their adsorption and thermochemistry properties, through ase-lib.org/ Atomic Simulation Environment (ASE)[36] package within the computational hydrogen electrode model (CHE).[30,37] The techniques and strategies used in this study are visually represented in the flowchart, Figure 1. In the following, we discuss and provide a concise summary of the key information for each step.

2.1. Total Energy Calculations. We perform spin-polarized DFT calculations,[38,39] within the generalized gradient approximation for the exchange-correlation energy functional as proposed by Perdew−Burke−Ernzerhof (PBE),[40] as implemented in the Vienna *ab initio* simulation package (VASP),[41,42] version 5.4.4. The interactions of core and valence electrons were described using the projected augmented wave (PAW) method.[43,44] Furthermore, we employed the pairwise semiempirical van der Waals D3 correction as proposed by Grimme[45] to improve the description of long-range van der Waals interactions in the adsorption process.[46,47]

The current study requires a substantial number of DFT calculations, approximately 700 calculations for various purposes. To reduce computational cost, our DFT calculations were performed in multiple phases, specifically (i) screening calculations followed by (ii) final optimization of selected configurations. In this framework, the Kohn−Sham orbitals were expanded into plane waves using varying cutoff energies tailored to the specific calculation level requirements, and these were aligned with the highest recommended cutoff energy ($\mathtt{ENMAX}_{max}$). For all calculations, a vacuum thickness of at least 20 Å was used to prevent periodic cell interactions in the z direction. Subsequently, we will elucidate our optimization parameters for each category of model systems.

2.1.1. TM_4@MoS_2 Substrates. As anticipated in previous studies,[48,49] the TM_4 clusters possess the ability to assume various structures, orientations, and adsorption sites in the 2D MoS_2 monolayer. Consequently, for cost-efficient computational screening, Γ-point calculations were performed to identify an initial set of lowest energy configurations, employing a plane wave cutoff energy of 0.875 × $\mathtt{ENMAX}_{max}$. The species considered in this analysis include TM, Mo, S, resulting in cutoffs of 301.800, 301.800, 312.658, and 364.909 eV for Fe_4@MoS_2, Co_4@MoS_2, Ni_4@MoS_2, and Cu_4@MoS_2, respectively. The convergence criterion for total energy was established at 10^{-4} eV, with the forces on individual atoms constrained to be less than 0.25 eV Å^{-1}, allowing all atoms to undergo relaxation. Subsequently, we selected for optimization all the structures whose total energies fall 5 meV/atom above the lowest energy. Next, we performed optimizations using plane wave cutoff energies obtained by 1.125 × $\mathtt{ENMAX}_{max}$, which yields the following cutoff energies: 388.028, 388.028, 401.988, 469.169 eV for Fe_4@MoS_2, Co_4@MoS_2, Ni_4@MoS_2, and Cu_4@MoS_2, respectively. Equilibrium configurations were obtained once the total energy convergence criterion reached 10^{-5} eV, and the forces on each atom were smaller than 0.025 eV Å^{-1}. All atoms were allowed to relax. In addition, we used a 3 × 3 × 1 k-mesh for the integration of the Brillouin zone, instead of only the Γ-point.

2.1.2. Adsorption on TM_4@MoS_2. Here, we use a similar procedure as before. For example, we perform Γ-point optimizations using a plane wave cutoff energy obtained from 0.875 × $\mathtt{ENMAX}_{max}$ for the selected species (H, C, O, TM, S, Mo), which yields a cutoff energy of 380.127 eV. The total energy convergence criterion was 10^{-4} eV, and the forces in each atom were less than 0.25 eV Å^{-1}. For these screening optimizations, only the adsorbate species were allowed to relax along the optimizations. After simulating the adsorption configurations, we selected for optimization those whose total energies were less than 5 meV/atom higher than the lowest energy. Subsequently, we performed optimizations of all atoms using a plane wave cutoff energy of 488.735 eV (1.125 × $\mathtt{ENMAX}_{max}$). Equilibrium configurations were obtained once the total energy convergence criterion was reached 10^{-5} eV, and the forces on each atom were smaller than 0.025 eV Å^{-1}. In addition, we used a 3 × 3 × 1 k-mesh for the integration of the Brillouin zone.

2.2. Design of the Atomic Structure Models. In this work, the geometric optimization of structures is based on local optimization algorithms,[50] where the initial molecular configurations have a significant influence on the result. For the 2D MoS_2 monolayer, we selected a 5 × 5 surface supercell. Thus, the use of a large supercell generates two distinct environments within the 2D MoS_2 substrate: a region characterized by the presence of V_S and a flat region far from the vacancy S. The subsequent discussion delineates the strategies employed for each category of substrates.

2.2.1. TM_4 Cluster Adsorption on MoS_2. To obtain our TM_4@MoS_2 substrate atomic models, we adsorbed TM_4 clusters on a previously optimized MoS_2 5 × 5 2D supercell including V_S. Due to the number of possible configurations of the clusters over the defective MoS_2, we employ the following strategy:

(1) First, we used the Xsorb package[34] to analyze the possible surface adsorption sites on the MoS_2 surface near (near-V_S) and far (far-V_S) from the V_S.
(2) Three initial configurations (planar, quasi-planar, and tetrahedral) of the cluster were considered and adsorbed on the surface sites screened from (*i*). We also accounted for rotational configurations of the cluster.
(3) Once we had obtained hundreds of structures, we used the *k*-means algorithm to cluster and filter similar structures to decrease the number of configurations before performing DFT calculations.

First, we performed these steps for the Cu_4@MoS_2 system, obtaining 90 initial configurations. This means that for each cluster symmetry (planar, quasi-planar, and tetrahedral), we choose 15 configurations near-V_S and 15 far-V_S. We used these structures to build the configurations for the remaining elements by replacing the TM atom sites. For these 360 structures, we first performed (i) low cutoff DFT calculations as described earlier and, subsequently, (ii) optimizing DFT calculations with a higher cutoff. From this final set of configurations, we selected the lowest energy system for each cluster-vacancy distance (far and near) and TM element, that is, in total we selected 8 TM_4@MoS_2 supports that we will use in the adsorption of chemical species. The energetic and geometric data for all substrates are provided in the electronic Supporting Information file.

2.2.2. Adsorption on TM_4@MoS_2. The adsorbed systems comprise the TM_4@MoS_2 substrates and adsorbates species

https://doi.org/10.1021/acscatal.5c05963
ACS Catal. 2025, 15, 20036−20048

(H, O, OH, CO, CHO, COH and OOH) on these substrates. To build these systems, we used the computational DockOnSurf package,[35] which generates the adsorption configurations on the support surface. We considered adsorption sites on the TM_4 cluster structure and sites on regions of the MoS_2 surface. Given the number of configurations, we first screened them using a low cutoff strategy and later selected a few configurations to optimize with higher cutoffs. All these procedures are illustrated in the flowchart in Figure 1.

2.3. Computational Hydrogen Electrode Model. We aim to study the performance of the TM_4@MoS_2 substrates upon adsorption of different adsorbates that are involved in the HER, OER, and CO_2RR reactions. To go beyond a simple total energy analysis, we will employ the CHE model to characterize the HER, OER, and CO_2RR reactions, providing powerful theoretical insights at reasonable computational costs.[30,37] In the CHE model, the equilibrium reaction,

$$H^+ + e^- \rightleftharpoons \frac{1}{2}H_{2(g)} \tag{1}$$

is a proton−electron coupled transfer (PCET), referenced to the reversible hydrogen electrode (RHE) by definition. Thus, it is considered at zero electrode potential (0 V versus RHE) for all pH and temperature. Once the reaction occurs and reaches equilibrium, its Gibbs free energy is zero ($\Delta G = 0$ eV). Hence, the calculation of the Gibbs free energy provides a very simple descriptor to characterize the redox reactions under these conditions. We can use the Gibbs free energy of the H_2 molecule in the gas phase $\left(\frac{1}{2}G(H_2)\right)$ to calculate the Gibbs free energy of any PCET step ($G(H^+ + e^-)$).

The Gibbs free energy is given as

$$G = E_{tot} + E_{ZPE} + \int_0^T C_p \, dT - TS \tag{2}$$

in which E_{tot} is the total energy, E_{ZPE} is the zero-point energy, C_p is the constant pressure heat capacity, T is the temperature, and S is the entropy term. It is worth mentioning that in eq 2, E_{tot} does not include solvent effects, and we have already neglected the term pV once it gives only small contributions ($\approx 10^{-3}$ meV).[51]

For an ideal gas, both C_p and S can be decomposed into translational, rotational, vibrational, and electronic components, with C_p having an additional term (k_B, Boltzmann constant) to switch from constant volume to constant pressure. For an adsorbate, the harmonic limit is considered, and thus, with no volume changes, and the system not performing pV work, we have $C_p = C_{V,vib}$. That is, only the constant volume heat capacity due to vibrational frequencies will be relevant. Then (harmonic limit):

$$\int_0^T C_p \, dT = \int_0^T C_{V,vib} \, dT = \sum_i \frac{\varepsilon_i}{e^{\varepsilon_i/k_B T} - 1} \tag{3}$$

where ε_i are the energies, given by $\varepsilon_i = h\omega_i$, with ω_i the vibrational frequencies, and the summation spans all degrees of freedom of the adsorbate. All parameters were obtained from DFT calculations. E_{tot} is obtained from a standard calculation, while the remaining terms come from vibrational frequency calculations and postprocessing using the ASE package.[36] Additional details on the form of vibrational and entropic terms are given elsewhere.[8,52,53]

The following equation obtains the Gibbs free energy of adsorption (ΔG_{ad}), that is, of a system upon the adsorption of a molecule:

$$\Delta G_{ad} = G_{tot}^{ads/sup} - (G_{tot}^{sup} + G_{tot,g}^{ads}) \tag{4}$$

in which $G_{tot}^{ads/sup}$, G_{tot}^{sup}, and $G_{tot,g}^{ads}$ are the Gibbs free energy for the total system, the clean substrate (support) and the molecule/adsorbate in the gas phase, respectively.

Here, we only considered the vibrational frequency modes of the adsorbate, which means that the support atoms are kept frozen during the vibrational calculations. Thus, we have the approximation $G_{tot}^{sup} = E_{tot}^{sup}$, with E_{tot}^{sup} the total energy of the substrate from DFT. Furthermore, $G_{tot,g}^{ads}$ is also calculated with the molecule in the gas phase, with hydrogen and oxygen referenced to the H_2 and O_2 molecules, respectively; that is, $G_{tot,g}^{H,O} \equiv \frac{1}{2}G_{tot,g}^{H_2,O_2}$. More details of the energetic contributions from vibrational calculations and each reaction to build the free-energy diagrams are given in the Supporting Information.

The overpotential (η) of a given electrochemical reaction, defined as the excess energy required to start product formation, can be measured experimentally. It is calculated as the difference between the onset and equilibrium potentials: $\eta = U_{onset} - U_{eq}$, in which U_{onset} is the applied potential at which the reaction begins, and U_{eq} is the equilibrium reaction potential. The equilibrium potential represents the minimum electrode potential needed to drive the reaction under standard conditions, for example, 0 V versus RHE for H_2 evolution and 1.23 V versus RHE for H_2O oxidation.

For a reaction involving n PCET steps, the onset potential can be given as

$$U_{onset} = \max\{\Delta G_i, \cdots, \Delta G_n\}/e \tag{5}$$

with ΔG_i the Gibbs free energy change of the i-th step and e the elementary charge. Recalling that $U_{eq} = 0$ V versus RHE for hydrogen evolution, the overpotential can be estimated within the CHE model by identifying the step with the highest Gibbs free energy change, once

$$\eta_{HER} = U_{onset} = \frac{|\Delta G_{H^*}|}{e} \tag{6}$$

This step is known as the potential-determining step (PDS). Both η and PDS are key properties for analyzing electrocatalytic performance in reactions such as HER, OER, and CO_2RR.

3. RESULTS AND DISCUSSION

This section is organized to elucidate the structural and energetic basis of the TM_4@MoS_2 substrates by examining their interaction with V_S, which encompasses geometric parameters, interaction energies, and deformation metrics. This analysis lays the groundwork for characterizing the catalytic activity. The section subsequently advances in a logical sequence to examine catalytic performance, starting with the HER, where Gibbs free energy diagrams and coordination trends elucidate the impact of cluster-vacancy proximity. This is succeeded by the OER, wherein step-by-step thermodynamics, overpotentials, and scaling relationships are meticulously detailed. Finally, the section addresses CO_2RR,

https://doi.org/10.1021/acscatal.5c05963
ACS Catal. 2025, 15, 20036−20048

Table 1. Geometric Parameters for TM_4 Clusters Adsorbed on the MoS_2 Monolayer[a]

Cluster	V_S	E_{int} (eV)	E_{int}^{vdW} (eV)	ECN (NNN)	d_{av} (Å)	$d_{CM}^{V_S}$ (Å)	$d_{CM,xy}^{V_S}$ (Å)	$d_{CM,z}^{V_S}$ (Å)	Ω	R_g (Å)
Fe_4	near	−7.03	−1.45	4.74	2.33	1.45	0.13	1.45	0.664	1.46
	far	−5.51	−1.22	4.89	2.32	6.72	6.47	1.79	0.665	1.49
Co_4	near	−7.92	−1.58	4.88	2.28	1.31	0.16	1.30	0.656	1.44
	far	−6.89	−1.42	4.56	2.26	6.90	6.71	1.61	0.665	1.52
Ni_4	near	−8.09	−1.72	5.11	2.31	1.36	0.01	1.36	0.671	1.43
	far	−8.67	−1.63	4.76	2.22	8.50	8.37	1.45	0.619	1.75
Cu_4	near	−6.99	−1.80	5.05	2.38	1.47	0.03	1.47	0.671	1.47
	far	−3.83	−1.43	3.74	2.37	6.32	5.95	2.13	0.598	1.66

[a]V_S indicates the configurational distance of the cluster from the sulfur vacancy. E_{int} and E_{int}^{vdW} are the interaction energies as given in eq 7 regarding the total energies and the vdW contributions, respectively. ECN and d_{av} are the effective coordination number and weighted average bond length, respectively, for the cluster atoms. $d_{CM}^{V_S}$, $d_{CM,xy}^{V_S}$, and $d_{CM,z}^{V_S}$ are the distances between the position of the center of mass (CM) of the cluster to the CM of the 6 sulfur atoms surrounding the vacancy site with xy and z the projected distance components along the xy plane and z (vertical) direction. Ω and R_g are the cluster sphericity and radius of gyration, respectively. More details on these measurements are given in the Supporting Information.

evaluating key intermediates, competitive reaction pathways, and poisoning effects to determine selectivity and practical viability. This structured methodology, which progresses from structure and stability to catalytic performance across three pivotal reactions, affords an in-depth understanding of how cluster-vacancy interactions can modulate reactivity.

3.1. Vacancy-Mediated Stabilization of Transition Metal Clusters. To improve the characterization of the substrates, we calculate several physicochemical properties, including the interaction energies of the TM_4 clusters in the MoS_2 monolayer, and several geometric parameters, namely, sphericity (Ω) and the radius of gyration (R_g) for the adsorbed clusters. The parameters $d_{CM}^{V_S}$, $d_{CM,xy}^{V_S}$, and $d_{CM,z}^{V_S}$ denote the distances between the center of mass (CM) of the cluster and the CM of the six closest S atoms that surround the V_S, with $d_{CM,xy}^{V_S}$ and $d_{CM,z}^{V_S}$ representing the distance projected onto the xy plane and the direction z, respectively. All results are summarized in Table 1.

3.1.1. Interaction Energies. To assess the energetic stability of the TM_4@MoS_2 substrates, we calculated the interaction energy (E_{int}) between the cluster and the MoS_2 surface as follows:

$$E_{int} = E_{tot}^{TM_4@MoS_2} - (E_{tot}^{MoS_2} + E_{tot}^{TM_4}) \quad (7)$$

Here, $E_{tot}^{TM_4@MoS_2}$ is the total energy of the final configuration for each TM_4 cluster, whether adsorbed near or far from the sulfur vacancy. $E_{tot}^{MoS_2}$ and $E_{tot}^{TM_4}$ are the total energies obtained by excluding the TM_4 and MoS_2 atoms, respectively, while maintaining their final configuration arrangements fixed. A similar strategy was used to calculate the contribution of van der Waals (vdW) to the interaction energy (E_{int}^{vdW}). Since all E_{int} values are negative, ranging from −3.83 eV to −8.67 eV, it indicates that all adsorbed systems (cluster + surface) are more stable than their isolated constituent parts, as expected due to structural distortions upon adsorption.

Adsorption near the V_S generally improved the stability of the system. For instance, Fe_4 showed an E_{int} of −7.03 eV (near) compared to −5.51 eV (far), and Co_4 had −7.92 eV (near) versus −6.89 eV (far). The only exception was the Ni_4@MoS_2 substrate, where the far-V_S configuration proved to be more stable (E_{int} of −8.67 eV) than the near-vacancy configuration (E_{int} of −8.09 eV). The near-V_S configurations exhibit smaller distances between the cluster's CM and the vacancy's CM: $d_{CM}^{V_S}$ values ranging from 1.31 to 1.47 Å, $d_{CM,xy}^{V_S}$ from 0.01 to 0.16 Å, and $d_{CM,z}^{V_S} \approx d_{CM}^{V_S}$. These values indicate that the cluster is effectively embedded within or directly atop the vacancy site, where the local atomic environment largely contributes to its stabilization.

In contrast, for far-V_S configurations, stability can be improved if electrostatic potential distortions due to the vacancy have a minimal impact on the cluster's structure. In fact, Freire et al.[54] showed that sulfur vacancies in 1H-TMDs have a more localized behavior, which contributes to decreasing the extent of potential distortions around them. For example, in the case of Ni_4@MoS_2, this stabilization occurs at a considerable distance of approximately 8.50 Å, which approaches the maximum possible distance ($d_{max} = a_0\sqrt{3}/3 = 9.14$ Å) within the plane xy, given a surface lattice parameter of a_0 = 15.83 Å.

In the gaseous state, clusters of the type TM_4 predominantly exhibit tetrahedral geometries, with Cu_4 being a notable exception, as it preferentially adopts a planar rhombic configuration.[55,56] Upon adsorption onto MoS_2, the Cu_4 cluster can stabilize in one of two configurations contingent upon its proximity to a sulfur vacancy (V_S). In the configuration far away from the V_S motif, the Cu_4 cluster retains a planar arrangement, albeit with significant distortion, characterized by a tetrahedral distortion parameter, Ω = 0.598, which deviates substantially from an ideal tetrahedron. This structural preference can be attributed to the inert nature of the MoS_2 basal plane. Conversely, in the proximity of a V_S, the Cu_4 cluster stabilizes in a structure reminiscent of a tetrahedron, possessing a distortion parameter of Ω = 0.671. This stabilization is facilitated by the local geometrical arrangement, whereby each transition metal atom forms bonds with two sulfur atoms encircling the vacancy site, comprising the tetrahedral base, and interacting with the local electrostatic potential. The fourth TM atom binds atop the base atoms, thus forming the tetrahedron structure.

3.1.2. The Role of the van der Waals Interactions. From our analysis, vdW interactions contribute substantially to the total interaction energy, ranging from −1.45 eV to −1.80 eV for E_{int}^{vdW}, that is, from 20 up to 40% to E_{int} in all systems. Puigdollers et al.[57] also observed a significant increase in adsorption energy for oxide systems when including vdW

https://doi.org/10.1021/acscatal.5c05963
ACS Catal. 2025, 15, 20036−20048

interactions, i.e., comparable enhancement magnitudes. Their analysis includes distinct vdW frameworks, namely DFT + D2 (pairwise) and vdW-DF (nonlocal vdW functional). Furthermore, they observed only slight changes in the adsorption geometry and no effects on the electronic structure by including vdW interactions.[57]

In the case of pairwise vdW correction, this significant contribution arises from the addition of additive vdW energy terms between the cluster atoms and the surface.[45,58] Furthermore, a more spread cluster, meaning atoms more distant from each other (indicated by a larger R_g), could correspond to a decrease in the magnitude of vdW interactions within the cluster. This trend is observed because pairwise van der Waals corrections are inversely proportional to r_{ij}, that is, $1/r_{ij}^n$ $(n = 6, 8, 10, \cdots)$, where r_{ij} is the distance between atoms, implying that greater atomic spreading (larger R_g) leads to smaller vdW contributions due to increased interatomic distances and structural distortions within the cluster. On the other hand, to compute E_{int}^{vdW}, we need to consider the pairwise contributions between the cluster and the surface, that is, it will depend on the nature of the elements and their distances. Most of the E_{int}^{vdW} accounts for 20% of E_{int}, indicating that despite small distortions, the systems have similar vdW interactions. The exception is for Cu_4 in the far-V_S configuration, which has a large R_g (1.66 Å), making the Cu atoms much closer to the surface, thus contributing to increasing E_{int}^{vdW}.

3.1.3. Cluster Deformation upon Adsorption. Upon adsorption on the MoS_2 monolayer, most of the TM_4 clusters largely retain a compact tetrahedral shape, characterized by Ω values around 0.660−0.670 and relatively small R_g values, even in the presence of a V_S. A notable exception is the Cu_4 cluster in the far-V_S configuration, which exhibits a more distorted structure with a lower sphericity (Ω = 0.598) and a larger radius of gyration (R_g = 1.66 Å), indicating greater atomic spreading. Interestingly, for both Ni_4 and Cu_4 clusters, interaction with the vacancy site resulted in structures that more closely resemble an ideal tetrahedron, with their Ω values for near-V_S being 0.671, the highest observed. Typically, near a vacancy, each of the three cluster atoms closest to the surface binds to two S atoms (in the center of a S hexagon), resulting in six total S neighbors. Far from the vacancy, the base of the cluster occupies the center of a triangle, resulting in only three S neighbors in total. Specifically, for Ni_4 and Cu_4, the three base atoms of the cluster form a coplanar arrangement when far away from V_S. In contrast, for Fe_4 and Co_4 in near-V_S configurations, one of the cluster atoms bends downward, disrupting coplanarity and leading to a deviation from the ideal Ω, as depicted in the side views of Figure 2 and reflected in their slightly lower Ω values (0.664 and 0.656, respectively) in Table 1. These observations are consistent with previous literature, where Nies and Nolan demonstrated that Cu_4 nanoclusters preferentially adsorb at the S top site and can undergo distortions when adsorbed on defective MoS_2.[48]

3.2. Thermodynamic Adsorption Properties. In this section, we summarize the energetic contributions to the final Gibbs free energies in the case of H adsorption. The same analysis was performed for the remaining adsorbates. As shown in eq 2, the Gibbs free energy is composed of at least four terms: (i) the electronic energy or total energy (E_{tot}), (ii) the zero-point energy (ZPE), (iii) the constant pressure heat capacity ($\int C_p\,dT$), and (iv) entropic contributions (TS). Once we are interested in energy differences, we can write

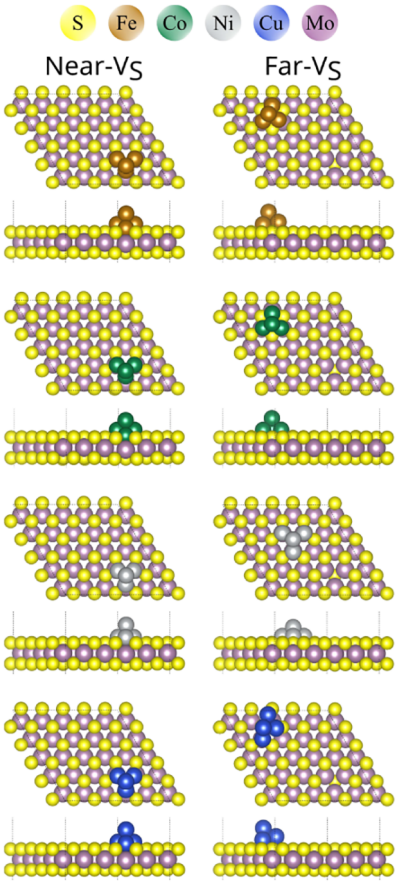

Figure 2. Lowest energy $TM_4@MoS_2$ substrates, including the configurations for near-V_S and far-V_S. The coloring of atoms is indicated.

$$\begin{aligned}\Delta G_{ad} &= \Delta E_{ad} + E_{corr} \\ &= \Delta E_{ad} + \Delta ZPE + \Delta\left(\int_0^T C_p\,dT\right) - T\Delta S\end{aligned} \tag{8}$$

where ΔE_{ad} is the difference in DFT (at T = 0 K) between reactants and products, that is, the adsorption energy, and E_{corr} = ΔZPE + $\Delta\int C_p\,dT - T\Delta S$ brings all the contributions of vibrational frequencies and finite temperature corrections, including the adsorbed and gas phase species. Through a mathematical derivation, we can obtain eq 4.

In addition, the adsorption of the reaction intermediates on the different substrates is defined as follows:

$$\Delta E_{ad} = E_{tot}^{ads/sup} - (E_{tot,g}^{ads} + E_{tot}^{sup}) \tag{9}$$

in which $E_{tot}^{ads/sup}$ is the total energy of the adsorbates upon adsorption in $TM_4@MoS_2$, $E_{tot,g}^{ads}$ is the total energies of the gas phase molecule and E_{tot}^{sup} is the total energy of the clean substrate.

In Figure 3, we summarize the energetic contributions to the Gibbs free energy for H adsorption. We can see that Fe_4, Co_4, and Ni_4 show similar ΔE_{ad} and ΔG_{ad}, suggesting comparable binding affinities. The most significant deviation arises from Cu_4 systems whose adsorption energy is highly sensitive to the coordination environment, ranging from weak to very strong

https://doi.org/10.1021/acscatal.5c05963
ACS Catal. 2025, 15, 20036−20048

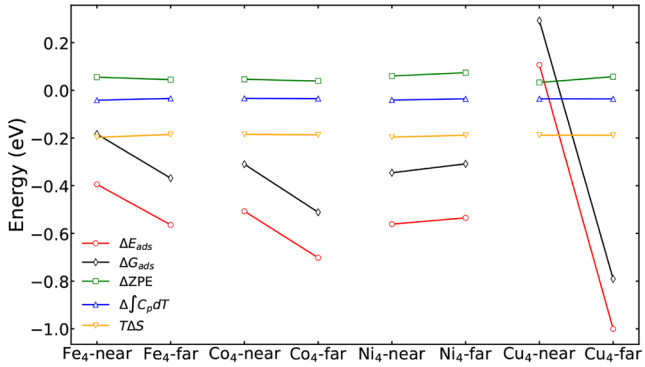

Figure 3. Gibbs free energy thermodynamic contributions for hydrogen adsorption on $TM_4@MoS_2$. The results here are relative to $1/2H_2$.

adsorption. Furthermore, for all systems, except Ni_4, the far-from-vacancy configurations result in more negative ΔE_{ad} and ΔG_{ad}, implying that the adsorbates are more stable when farther from the vacancy. This effect is most prominent for Cu_4, indicating a stronger electronic or geometric influence. In turn, the Ni_4 systems exhibit the smallest variation in adsorption and Gibbs free energy, indicating the weakest sensitivity to the local environment.

In the case of the thermodynamic corrections, we can see that ΔZPE and $\Delta\left(\int_0^T C_p\, dT\right)$ have small and relatively constant values for all systems. In fact, the mean values for ΔZPE and $\Delta\left(\int_0^T C_p\, dT\right)$ are 0.051 eV and −0.036 eV with small standard deviations of 0.013 and 0.003 eV, respectively. Furthermore, they do not contribute significantly to ΔG_{ad} variations. On the other hand, the entropy correction ($T\Delta S$) dominates the correction terms in magnitude, with a mean value of −0.189 eV, and also with a small variation between the systems, with a standard deviation of 0.005 eV. Note that with such small variations, the correction terms exhibit system-independent behavior.

Finally, we can see that ΔE_{ad} is the dominant term in the computation of ΔG_{ad}, with the primary difference between them coming from the term TΔS, which presents only small variations. For example, a similar result was obtained by Nørskov et al.[59] while studying H adsorption on metallic surfaces. At the time, they used a constant value as representative for all systems to obtain the Gibbs free energy from the adsorption energy, that is, $\Delta G_{H^*} = \Delta E_H + 0.24$ (eV), in which ΔG_{H^*} and ΔE_H are the Gibbs free energy and the H adsorption energy, and the constant 0.24 eV includes all thermodynamic corrections. In this sense, we can realize that for these systems, ΔG_{ad} and ΔE_{ad} differ only by a small energy shift, and the latter dictates the energetic trends.

3.3. Hydrogen Evolution Reaction. HER is a fundamental half-cell reaction in electrochemical H_2O splitting, where H^+ is reduced to H_2 at the cathode. In acidic media, HER proceeds through a two-electron transfer mechanism, following the Volmer−Tafel or Volmer−Heyrovsky pathway. The initial step involves the adsorption of a $H^+ + e^-$ onto the catalyst surface to form an adsorbed hydrogen intermediate (H*), i.e., a process known as the Volmer step. This is followed by the combination of two adsorbed species H* to release H_2 (Tafel step), or by electrochemical desorption involving another electron and proton (Heyrovsky step).[59]

Figure 4 shows the Gibbs free energy of adsorption of H, ΔG_{H^*}, for different $TM_4@MoS_2$ substrates. Mostly, the results

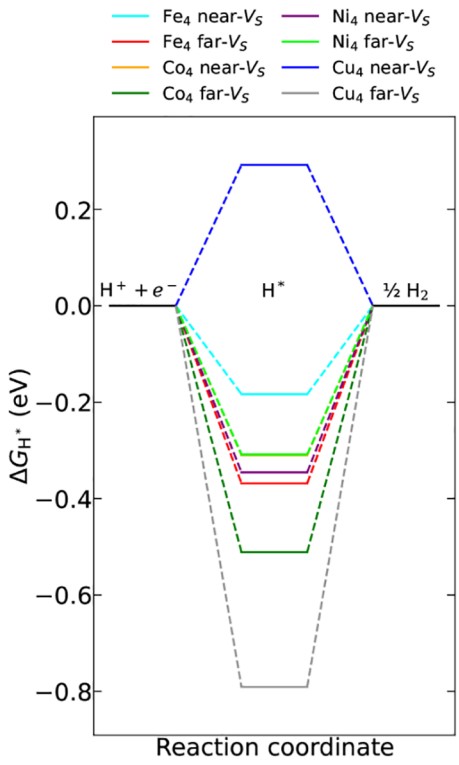

Figure 4. Hydrogen evolution reaction free energy diagram for all substrates. The results here are relative to $1/2H_2$. In the reaction coordinate, we represent the free energies of each step in the overall reaction, the PCET step, the intermediate state (H*), and the final H_2 evolution.

fall within the ± 0.4 eV energy range. For Pt(111) ($3 \times 3 \times 1$ with 5 atomic layers slab, 15 Å vacuum) our calculated ΔG_{H^*} energies for topsite is −0.38 eV. We may find it ≈0.2 eV in the literature.[60,61] Thus, according to Sabatier's principle[62] these substrates would work satisfactorily for HER. The best results were for $Fe_4@MoS_2$ with the cluster near-V_S. Given the low coordination of the cluster structure, it is expected that the adsorbates will prefer to bind to the surface through the cluster site. The adsorption sites are bridge-like in most cases, with the effective coordination number (ECN)[63] of the adsorbate varying from 2.85 to 4.64 nearest neighbors, and the weighted bond length (d_{av}) from 1.62 Å to 1.75 Å.

Within the context of the CHE model, hydrogen adsorption is conventionally represented by a singular hydrogen atom. Nevertheless, in the scenario involving metal clusters, the adsorption of multiple hydrogen atoms can occur concurrently, and diatomic hydrogen molecules are capable of direct interaction with the adsorption sites.[64,65] The augmentation of cluster structures through hydrogen adsorption has the potential to facilitate hydrogen spillover. This refers to the diffusion process of hydrogen atoms from the metal cluster to the underlying support material, such as MoS_2, which may ultimately result in hydrogen desorption.[64,66] Recent empirical investigations have underscored the critical role of structural defects in enhancing hydrogen spillover mechanisms.[67,68] Specifically, research by Du et al. has elucidated that sulfur vacancies in MoS_2 amplify this phenomenon by reducing the work function at the metal−support juncture.[68] Consequently,

https://doi.org/10.1021/acscatal.5c05963
ACS Catal. 2025, 15, 20036−20048

this enhancement contributes to improved hydrogen production efficiency.[68,69] Despite these advancements, there remain substantial challenges in deciphering the underlying mechanisms governing hydrogen spillover and in achieving its experimental characterization.[64,69−72] A deeper understanding requires explicit modeling of multihydrogen coverage and dynamic interactions, which are beyond the ambit of the current investigation.

In general, the near-V_S structures presented the best results, except for Ni_4@MoS_2, but with a slight energy difference between near- and far-V_S configurations. We can already realize that V_S helps to improve HER reactivity. In case of Ni_4@MoS_2 far-V_S, the more stable configuration of the substrate compared to near-V_S contributed to achieving a smaller ΔG_{H^*}. The largest ΔG_{H^*} was obtained for Cu_4@MoS_2 far-V_S configuration with almost −0.8 eV, indicating a strong bonding of H with the cluster. Looking at geometric adsorption properties, we can see that the far- and near-V_S configurations for this system do not differ largely, and the same holds for the other TM_4 clusters. Hence, proximity with V_S plays an important role in the adsorption energetics and the local electronic structure.

In terms of geometric distortion, we have already seen that Cu_4@MoS_2 far-V_S systems have a planar-like geometry, decreasing coordination and contributing to increasing ΔG_{H^*}. After adsorption, the cluster structure undergoes slight changes, decreasing Ω and increasing R_g. Thus, it tends to an even more planar configuration, which may affect the adsorption properties if higher hydrogen coverages are considered. For the single Cu atom supported in defective MoS_2, Liu et al. found $\Delta G_{H^*} = -0.2$ eV.[73] However, in their work, in addition to considering a single atom, they used a 2 × 2 supercell with two MoS_2 layers. In contrast to our results, we can state that considering larger clusters and supercells has a great impact on HER activity, especially considering near and far V_S. From our data, we can illustrate a key principle in modern catalyst design: performance is determined not only by the active metal itself but also by the synergistic interaction between the metal and its support environment.[74−76] Here, defect engineering is shown to be a highly effective strategy for tuning the catalytic properties of metal clusters to achieve near-optimal performance for HER.

3.4. Oxygen Evolution Reaction. The OER is characterized by the overarching chemical equation below,

$$2H_2O_{(l)} \rightarrow O_{2_{(g)}} + 4H^+ + 4e^- \quad U_0 = 1.23 \text{ V vs RHE} \tag{10}$$

The OER is a four-electron process that occurs in multiple steps. Within the CHE model, the free energy of OER is obtained through the reaction intermediates OH, O, and OOH, which are proton-coupled electron transfer reaction steps, so charge neutrality is maintained.[62] These reaction steps are given as follows,

$$H_2O_{(l)} + {}^* \rightarrow OH^* + H^+ + e^- \qquad \Delta G_1 \tag{11}$$

$$OH^* \rightarrow O^* + H^+ + e^- \qquad \Delta G_2 \tag{12}$$

$$O^* + H_2O_{(l)} \rightarrow OOH^* + H^+ + e^- \qquad \Delta G_3 \tag{13}$$

$$OOH^* \rightarrow {}^* + O_{2(g)} + H^+ + e^- \qquad \Delta G_4 \tag{14}$$

In these equations, ∗ denotes the surface active site of the catalyst, and OH*, O*, and OOH* denote the adsorbed molecular species (reaction intermediates). For an ideal catalyst, at the equilibrium potential, there must be no thermodynamic barrier between the reaction steps. In terms of thermodynamic criteria, this means that $\Delta G_1 = \Delta G_2 = \Delta G_3 = \Delta G_4 = 0$ eV in $U = 1.23$ V vs RHE, while in the CHE framework, this means $\Delta G_1 = \Delta G_2 = \Delta G_3 = \Delta G_4 = 1.23$ eV in $U = 0.00$ V vs RHE.[62]

In Figure 5, we show our results on the OER reaction steps for each TM_4@MoS_2 substrate, indicating their PDSs and

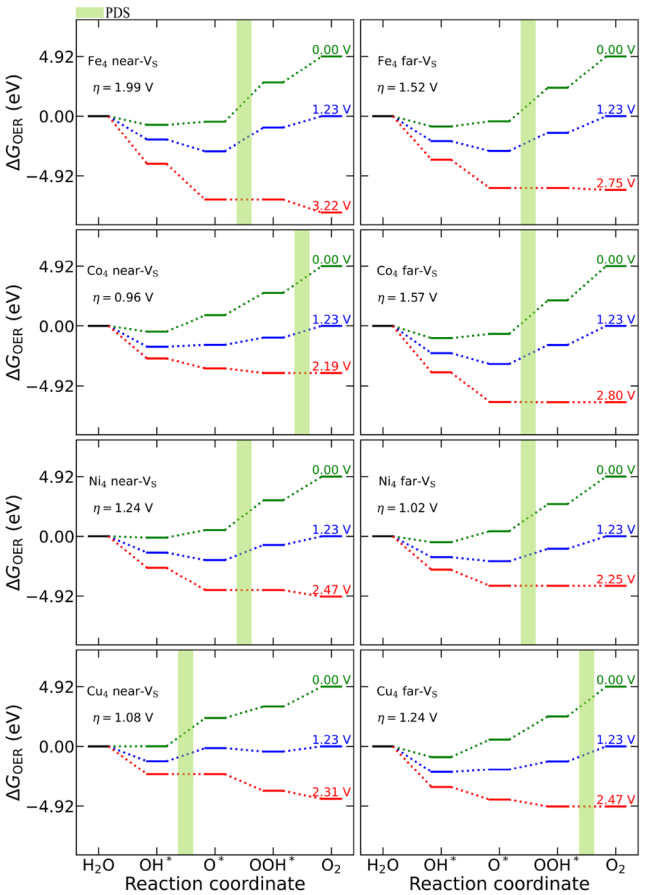

Figure 5. Oxygen evolution reaction free energy given at different electrode potentials. Along the reaction coordinate, we provide the free energies of each intermediate step in the process toward the O_2 evolution. The results here are relative to H_2O.

overpotentials. For example, in Figure 5 the green (blue) steps represent the OER at $U = 0.00$ V (1.23 V) versus RHE, while the red steps represent the OER at the overpotential versus RHE. By applying potentials from 0.00 V to η V throughout the system, the reaction steps will decrease toward the evolution of O_2. When η V is applied, the last step downhill will be the system's PDS (also the largest free energy change). In other words, the change in free energy between two consecutive reaction intermediates approaches zero, as indicated by the light green stripes in Figure 5.

At first, there are no clear trends in the behavior of ΔG_{OER}. The overpotentials vary from 0.95 to 2.00 V including all systems, with the smallest (largest) value for Co_4@MoS_2 near-V_S (Fe_4@MoS_2 near-V_S). In the near-V_S cases, the PDSs are ΔG_3 for Fe_4@MoS_2 and Ni_4@MoS_2; ΔG_4 for Co_4@MoS_2; and ΔG_2 for Cu_4@MoS_2. On the other hand, for far-V_S systems, the PDSs occur for ΔG_3, except for Cu_4@MoS_2, where the

https://doi.org/10.1021/acscatal.5c05963
ACS Catal. 2025, 15, 20036−20048

PDS is for ΔG_4. This last behavior can be rationalized by the larger distortions observed for Cu_4@MoS_2, inducing a more planar configuration, thus favoring another reaction step.

Co_4@MoS_2 near-V_S has the lowest overpotential among the materials investigated and thus should present the best catalytic performance. On the other hand, the overpotentials for the Ni_4@MoS_2 and Cu_4@MoS_2 systems are not too high, ranging from 1.00 to 1.20 V, and could be possible candidates for the OER process. The overpotentials for Fe_4@MoS_2 and Ni_4@MoS_2 are larger for near-V_S structures compared to far-V_S ones, but they have the same PDSs. Structurally, the ECNs for oxygen (O* step) in the near-V_S configurations are larger than those for far-V_S, making it more stable (or less reactive), thus increasing the energy needed to proceed to the next reaction step. In addition, local electrostatic effects may contribute to this mechanism.

However, in real-world applications, experimental control of the behavior of the intermediates can be challenging, and the materials deviate from the ideal catalyst. Thus, finding correlations between the properties of the materials can help determine their potential as catalysts. These so-called scaling relationships can help to describe the catalyst behavior, reducing the problem dimensionality to only one free parameter. For example, the scaling relationship between OH* and OOH* has been found to follow a universal trend for planar metal oxides[62,77] exhibiting a linear correlation, given by the following equation,

$$\Delta G_2 + \Delta G_3 = 3.2 \text{ eV} \tag{15}$$

or, equivalently,

$$\Delta G_{OOH^*} - \Delta G_{OH^*} = 3.2 \text{ eV} \tag{16}$$

Here, we have found a behavior similar to that presented in eq 16, indicating that this could be a trend for other materials' families, not only for oxides; see Figure 6.

3.5. CO_2 Reduction Reaction. Initially, to investigate CO_2RR, we must consider competing reactions such as HER and surface poisoning with OH, which can decrease performance toward CO_2RR and more reduced carbon products.[31] Hence, as pointed out by Neto et al.,[8] at least four criteria must be followed to obtain potential catalysts for CO_2RR: (i) avoiding CO* desorption by strongly binding CO to the surface; (ii) obtaining a small $G_{CHO^*(COH^*)} - G_{CO^*}$ energy difference favoring the first reduction of CO*; (iii) the OH adsorption should be weak enough; and (iv) the HER should not dominate, that is, should not be thermodynamically favored.

In Figure 7, we show the free energy diagram for the desorption of CO and CO_2RR reaction intermediates, further compared to competing reactions. Within the mechanism CO_2RR, CO_2 first adsorbs on the surface and reduces to CO*, and from that the reaction can evolve to desorption of CO or further reduced species (COH*, CHO*),[8] CO* should be our reference step. We observe that hydrogenation to CHO is the most favorable, except for the Cu_4 near-V_S, where the CO desorption is more favorable. In turn, hydrogenation to COH presents larger free energies, but excepting Co_4, Ni_4, and Cu_4 near-V_S configurations, all the systems would favor COH* against CO desorption.

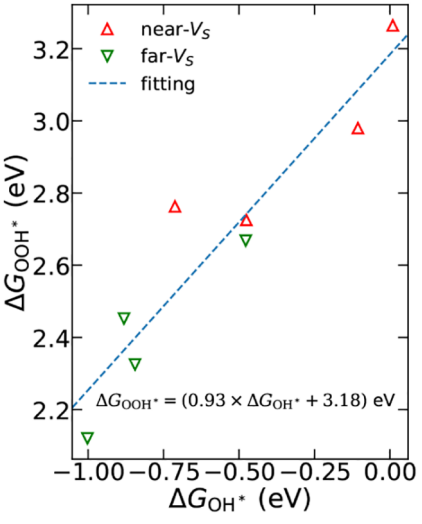

Figure 6. Oxygen evolution reaction scaling relation for ΔG_{OOH^*} and ΔG_{OH^*}. The fitting is shown to compare the expected and real values.

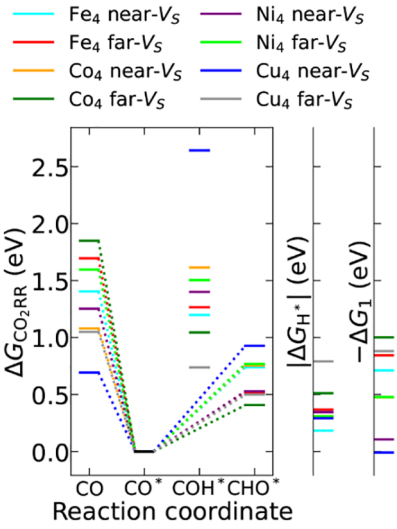

Figure 7. CO_2RR Free energy for all systems, relative to CO*. We display an additional y axis for HER and OH poisoning, which are important for discussing selectivity. From the intermediate CO*, the system may follow either to CO desorption or to further reducing CO to value-added species (COH*, CHO*).

Looking at the energies of the intermediate reaction CHO*, there is a small energy separation between the far- and near-V_S configurations, except for Ni_4. That is, for CHO* the energies for far-V_S configurations are below ≈ 0.52 eV, while those above ≈ 0.73 eV correspond to near-V_S configurations. In principle, these preliminary findings indicate that these systems may be suitable for CO_2RR, with far-V_S configurations that favor C reduction toward CHO*. Based on that, the most promising catalysts are Co_4 far-V_S and Cu_4 far-V_S.

For a more complete analysis, we have to consider competing reactions: (i) HER dominates (energies closer to zero) for almost all cases, except Co_4 far-V_S and Cu_4 far-V_S. (ii) The OH poisoning is also likely to occur in most systems, e.g., for Co_4 far-V_S and Cu_4 far-V_S, leading us to conclude that, unfortunately, these systems can be problematic if applied to CO_2RR; for Cu_4 near-V_S and Ni_4 near-V_S, poisoning with OH is less likely to occur and formation of H_2O is the tendency. In summary, these systems are better candidates for HER/OER instead of CO_2RR. Wang et al. showed that Fe_3 clusters anchored to MoS_2 with V_S had excellent catalytic performance

https://doi.org/10.1021/acscatal.5c05963
ACS Catal. 2025, 15, 20036−20048

to CO_2RR, which is in close agreement with our results. Their results and our work (TM_4) systematically show that activity MoS_2 can be tuned with clusters and appears to be highly dependent on the size of the cluster.[78] Particularly, this is an important insight, as controlling the growth of the size of the cluster on substrates can be experimentally challenging. However, issues regarding selectivity remain significant.

4. CONCLUSIONS

In this study, we combined density functional theory calculations and the computational hydrogen electrode model to investigate the catalytic efficiency of the hydrogen evolution, oxygen evolution, and carbon dioxide reduction reactions on substrates characterized by the presence of transition-metal tetramer clusters (Fe_4, Co_4, Ni_4, and Cu_4) supported on pristine and defective (sulfur vacancies) MoS_2 monolayers, which opens the opportunity to explore the presence of synergistic effects.

With the exception of Ni_4, all TM_4 clusters demonstrate a preferential anchoring near V_S sites, where they exhibit enhanced binding stability and largely retain compact tetrahedral geometries. The Cu_4 cluster constitutes a notable exception, undergoing significant structural distortions when situated away from the vacancy. As expected from previous studies, van der Waals interactions contribute up to 40% of the total binding energy of the clusters to the substrate, especially in compact configurations, highlighting their substantial role in stabilizing supported clusters. The interaction between cluster flexibility, local coordination, and the electronic perturbations introduced by V_S is crucial in modulating adsorption strength and, consequently, direct effects on the catalytic performance.

For the hydrogen evolution reaction, several configurations demonstrate Gibbs free energy changes (ΔG_{H^*}) within the thermoneutral range (i.e., ±0.4 eV), which is indicative of effective catalytic activity. Among these configurations, Fe_4@MoS_2 positioned near a sulfur vacancy is identified as the most promising system. This is attributed to its optimized hydrogen adsorption energetics and enhanced electronic coupling with the defect site. In the context of the oxygen evolution reaction, the calculated overpotentials span from 0.95 to 2.00 V, with Co_4@MoS_2 near a sulfur vacancy exhibiting the lowest overpotential. A linear scaling relationship is observed between the Gibbs free energy changes of the hydroxide (ΔG_{OH^*}) and hydroperoxide (ΔG_{OOH^*}) intermediates. This observation suggests that the design principles traditionally applied to oxide catalysts can also be appropriately extended to systems based on chalcogenides.

In the context of CO_2 reduction reactions, the majority of metal clusters exhibit a preference for the hydrogenation of CO to form CHO. An exception to this trend is observed with the Cu_4@MoS_2 clusters proximal to near-V_S sites, which demonstrate a tendency to facilitate the desorption of CO. Meanwhile, Co_4 and Cu_4 clusters positioned at locations distant from vacancies manifest moderately favorable energetic profiles for the hydrogenation of CO_2; however, their selectivity is significantly compromised due to the competitive hydrogen evolution reaction activity and surface poisoning by hydroxide intermediates. These findings underscore the kinetic and thermodynamic challenges associated with CO_2 conversion processes on MoS_2-supported transition-metal clusters.

Therefore, our study elucidates that the electronic characteristics inherent to transition metals, in conjunction with the presence of sulfur vacancies, collaboratively influence the structural stability and catalytic properties of TM_4@MoS_2 systems. The integration of tiny clusters with 2D chalcogenide substrates signifies a promising avenue for the development of efficient and earth-abundant electrocatalysts. The strategies of defect engineering and cluster configuration optimization emerge as pivotal methodologies for precisely modulating activity and selectivity across a spectrum of electrochemical reactions. These findings provide critical insights for the rational design of advanced materials aimed at sustainable energy conversion.

■ ASSOCIATED CONTENT

Data Availability Statement

As mentioned, all DFT calculations were done using the VASP package, which can be used under a nonfree academic license. Furthermore, additional details are provided within the Supporting Information, while additional raw data can be obtained directly from the authors upon request. Our group also provides the data in the https://data.mendeley.com/ Mendeley Data Repository, where it is listed under the same title as this work.

Supporting Information

The Supporting Information is available free of charge at https://pubs.acs.org/doi/10.1021/acscatal.5c05963.

Theoretical and computational details, the convergence of computational parameters for pristine and S-deficient 1H-MoS_2 monolayers, such as lattice parameters, total energy, band gap, and coordination numbers; results for the adsorption of small molecules (PDF)

■ AUTHOR INFORMATION

Corresponding Author

Juarez L. F. Da Silva − *São Carlos Institute of Chemistry, University of São Paulo, São Carlos, São Paulo 13560-970, Brazil;* orcid.org/0000-0003-0645-8760; Email: juarez_dasilva@iqsc.usp.br

Authors

Rafael L. H. Freire − *São Carlos Institute of Chemistry, University of São Paulo, São Carlos, São Paulo 13560-970, Brazil;* orcid.org/0000-0002-4738-3120

Henrique A. B. Fonseca − *São Carlos Institute of Chemistry, University of São Paulo, São Carlos, São Paulo 13560-970, Brazil*

Pedro Ivo R. Moraes − *São Carlos Institute of Chemistry, University of São Paulo, São Carlos, São Paulo 13560-970, Brazil;* orcid.org/0000-0001-7339-5945

Mauricio Mocelim − *São Carlos Institute of Chemistry, University of São Paulo, São Carlos, São Paulo 13560-970, Brazil;* orcid.org/0000-0002-4683-7223

Marionir M. C. B. Neto − *São Carlos Institute of Chemistry, University of São Paulo, São Carlos, São Paulo 13560-970, Brazil;* orcid.org/0000-0001-8032-4168

Complete contact information is available at: https://pubs.acs.org/10.1021/acscatal.5c05963

Funding

The Article Processing Charge for the publication of this research was funded by the Coordenacao de Aperfeicoamento de Pessoal de Nivel Superior (CAPES), Brazil (ROR identifier: 00x0ma614).

Notes

The authors declare no competing financial interest.

■ ACKNOWLEDGMENTS

The authors appreciate the support from FAPESP (São Paulo Research Foundation) and Shell, project numbers 2017/11631-2 and 2018/21401-7 and the strategic importance of the support provided by ANP (Brazil's National Oil, Natural Gas and Biofuels Agency). The authors also thank the infrastructure provided to our computer cluster by the Department of Information Technology - Campus São Carlos. The research was developed with the help of HPC resources provided by the Information Technology Superintendence of the University of São Paulo. H. A. B. Fonseca, P. I. R. Moraes, and M. Mocelim acknowledge FAPESP for financial support, grant numbers 2021/05728-9, 2023/12824-0, and 2023/15357-3. We acknowledge the use of advanced language models for their assistance in English-language editing, grammar revision, and text refinement.

■ ABBREVIATIONS

DFT	Density functional theory
2D	Two-dimensional
VASP	Vienna Ab initio Simulation package
PBE	Perdew−Burke−Ernzerhof
PAW	Projector augmented-wave

■ REFERENCES

(1) Olabi, A. G.; Elsaid, K.; Obaideen, K.; Abdelkareem, M. A.; Rezk, H.; Wilberforce, T.; Maghrabie, H. M.; Sayed, E. T. Renewable Energy Systems: Comparisons, Challenges and Barriers, Sustainability Indicators, and the Contribution to UN Sustainable Development Goals. *Int. J. Thermofluids* **2023**, *20*, 100498.

(2) Hassan, Q.; Viktor, P.; Al-Musawi, J. T.; Mahmood Ali, B.; Algburi, S.; Alzoubi, H. M.; Khudhair Al-Jiboory, A.; Zuhair Sameen, A.; Salman, H. M.; Jaszczur, M. The Renewable Energy Role in the Global Energy Transformations. *Renew. Energy Focus* **2024**, *48*, 100545.

(3) Zou, X.; Zhang, Y. Noble Metal-free Hydrogen Evolution Catalysts for Water Splitting. *Chem. Soc. Rev* **2015**, *44*, 5148−5180.

(4) Zeng, M.; Li, Y. Recent Advances in Heterogeneous Electrocatalysts for the Hydrogen Evolution Reaction. *J. Mater. Chem. A* **2015**, *3*, 14942−14962.

(5) Song, J.; Wei, C.; Huang, Z.-F.; Liu, C.; Zeng, L.; Wang, X.; Xu, Z. J. A Review on Fundamentals for Designing Oxygen Evolution Electrocatalysts. *Chem. Soc. Rev* **2020**, *49*, 2196−2214.

(6) Plevová, M.; Hnát, J.; Bouzek, K. Electrocatalysts for the Oxygen Evolution Reaction in Alkaline and Neutral Media. A Comparative Review. *J. Power Sources* **2021**, *507*, 230072.

(7) Yaashikaa, P. R.; Senthil Kumar, P.; Varjani, S. J.; Saravanan, A. A Review on Photochemical, Biochemical and Electrochemical Transformation of CO_2 into Value-Added Products. *J. CO2 Util* **2019**, *33*, 131−147.

(8) Neto, M. M. C. B.; Verga, L. G.; Da Silva, J. L. F.; Galvão, B. R. L. Computational Screening of Silver-based Single-atom Alloys Catalysts for CO_2 Reduction. *J. Chem. Phys* **2024**, *160*, 094706.

(9) Senftle, T. P.; Carter, E. A. The Holy Grail: Chemistry Enabling an Economically Viable CO_2 Capture, Utilization, and Storage Strategy. *Acc. Chem. Res* **2017**, *50*, 472−475.

(10) Fonseca, H. A. B.; Verga, L. G.; Da Silva, J. L. F. Theoretical Tuning of the Cu/S Ratio on Two-Dimensional CuS_x Materials for the CO_2 Electrochemical Reduction Reaction. *J. Phys. Chem. C* **2023**, *127*, 24118−24128.

(11) Verga, L. G.; Wang, Y.; Chakraborty, T.; Da Silva, J. L. F.; Mueller, T. The Effects of Near-Surface Atomic Order on the Catalytic Properties of Cu_3Au and $CuAu_3$ Intermetallics for the CO_2 Reduction Reaction. *Catal. Sci. Technol* **2023**, *13*, 6415−6430.

(12) Chen, T.-W.; Chen, S.-M.; Anushya, G.; Kannan, R.; Al-Sehemi, A. G.; Alargarsamy, S.; Gajendran, P.; Ramachandran, R. Development of Different Kinds of Electrocatalyst for the Electrochemical Reduction of Carbon Dioxide Reactions: An Overview. *Molecules* **2023**, *28*, 7016.

(13) Irshad, H.; Zia, M.; Al-Hajri, R.; Khattak, Z. A. K.; Al-Abri, M.; Ahmad, N.; Younus, H. A. Electrocatalysts for Hydrogen and Oxygen Evolution Reactions Under Neutral/Near-Neutral Conditions: Summary and Challenges. *Int. J. Hydrogen Energy* **2025**, *137*, 1009−1041.

(14) Anwar, S.; Khan, F.; Zhang, Y.; Djire, A. Recent Development in Electrocatalysts for Hydrogen Production Through Water Electrolysis. *Int. J. Hydrogen Energy* **2021**, *46*, 32284−32317.

(15) Mano, P.; Jitwatanasirikul, T.; Roongcharoen, T.; Takahashi, K.; Namuangruk, S. Tuning Covalent Bonding of Single Transition Metal Atom Doped in S Vacant MoS_2 for Catalytic CO_2 Reduction Reaction Product Selectivity. *Appl. Surf. Sci* **2025**, *688*, 162339.

(16) Py, M. A.; Haering, R. R. Structural Destabilization Induced by Lithium Intercalation in MoS_2 and Related Compounds. *Can. J. Phys* **1983**, *61*, 76−84.

(17) Eda, G.; Fujita, T.; Yamaguchi, H.; Voiry, D.; Chen, M.; Chhowalla, M. Coherent Atomic and Electronic Heterostructures of Single-Layer MoS_2. *ACS Nano* **2012**, *6*, 7311−7317.

(18) Calandra, M. Chemically Exfoliated Single-Layer MoS_2: Stability, Lattice Dynamics, and Catalytic Adsorption from First Principles. *Phys. Rev. B* **2013**, *88*, 245428.

(19) Samy, O.; El Moutaouakil, A. A Review on MoS_2 Energy Applications: Recent Developments and Challenges. *Energies* **2021**, *14*, 4586.

(20) Jaramillo, T. F.; Jørgensen, K. P.; Bonde, J.; Nielsen, J. H.; Horch, S.; Chorkendorff, I. Identification of Active Edge Sites for Electrochemical H_2 Evolution from MoS_2 Nanocatalysts. *Science* **2007**, *317*, 100−102.

(21) Benck, J. D.; Hellstern, T. R.; Kibsgaard, J.; Chakthranont, P.; Jaramillo, T. F. Catalyzing the Hydrogen Evolution Reaction (HER) with Molybdenum Sulfide Nanomaterials. *ACS Catal* **2014**, *4*, 3957−3971.

(22) Meng, C.; Chen, X.; Gao, Y.; Zhao, Q.; Kong, D.; Lin, M.; Chen, X.; Li, Y.; Zhou, Y. Recent Modification Strategies of MoS_2 for Enhanced Electrocatalytic Hydrogen Evolution. *Molecules* **2020**, *25*, 1136.

(23) Kim, J.; Park, A.; Kim, J.; Kwak, S. J.; Lee, J. Y.; Lee, D.; Kim, S.; Choi, B. K.; Kim, S.; Kwag, J.; Kim, Y.; Jeon, S.; Lee, W. C.; Hyeon, T.; Lee, C.-H.; Lee, W. B.; Park, J. Observation of H_2 Evolution and Electrolyte Diffusion on MoS_2 Monolayer by In Situ Liquid-Phase Transmission Electron Microscopy. *Adv. Mater* **2022**, *34*, 2206066.

(24) Mohanty, B.; Ghorbani-Asl, M.; Kretschmer, S.; Ghosh, A.; Guha, P.; Panda, S. K.; Jena, B.; Krasheninnikov, A. V.; Jena, B. K. MoS_2 Quantum Dots as Efficient Catalyst Materials for the Oxygen Evolution Reaction. *ACS Catal* **2018**, *8*, 1683−1689.

(25) Ouyang, Y.; Ling, C.; Chen, Q.; Wang, Z.; Shi, L.; Wang, J. Activating Inert Basal Planes of MoS_2 for Hydrogen Evolution Reaction through the Formation of Different Intrinsic Defects. *Chem. Mater* **2016**, *28*, 4390−4396.

(26) Tsai, C.; Li, H.; Park, S.; Park, J.; Han, H. S.; Nørskov, J. K.; Zheng, X.; Abild-Pedersen, F. Electrochemical Generation of Sulfur Vacancies in the Basal Plane of MoS_2 for Hydrogen Evolution. *Nat. Commun* **2017**, *8*, 1−8.

(27) Hu, J.; Yu, L.; Deng, J.; Wang, Y.; Cheng, K.; Ma, C.; Zhang, Q.; Wen, W.; Yu, S.; Pan, Y.; Yang, J.; Ma, H.; Qi, F.; Wang, Y.; Zheng, Y.; Chen, M.; Huang, R.; Zhang, S.; Zhao, Z.; Mao, J.; Meng, X.; Ji, Q.; Hou, G.; Han, X.; Bao, X.; Wang, Y.; Deng, D. Sulfur Vacancy-rich MoS_2 as a Catalyst for the Hydrogenation of CO_2 to Methanol. *Nat. Catal* **2021**, *4*, 242−250.

https://doi.org/10.1021/acscatal.5c05963
ACS Catal. 2025, 15, 20036−20048

(28) Zou, F.; Zhu, L.; Gao, G.; Wu, M.; Yao, K. Temperature-controlled Spin Filter and Spin Valve Based on Fe-doped Monolayer MoS_2. *Phys. Chem. Chem. Phys* **2016**, *18*, 6053−6058.
(29) Basak, A.; Das, D.; Sen, D.; Chattopadhyay, K. K. Theoretical Insights into the Electronic and Magnetic Behaviors of the Metal Substituted 1H-MoS_2 Systems: Their Potential Towards CO Adsorption and Sensing. *Comput. Mater. Sci* **2014**, *95*, 399−407.
(30) Nørskov, J. K.; Rossmeisl, J.; Logadottir, A.; Lindqvist, L.; Kitchin, J. R.; Bligaard, T.; Jónsson, H. Origin of the Overpotential for Oxygen Reduction at a Fuel-cell Cathode. *J. Phys. Chem. B* **2004**, *108*, 17886−17892.
(31) Peterson, A. A.; Nørskov, J. K. Activity Descriptors for CO_2 Electroreduction to Methane on Transition-metal Catalysts. *J. Phys. Chem. Lett* **2012**, *3*, 251−258.
(32) Kumar, K.; Jamnuch, S.; Majidi, L.; Misal, S.; Ahmadiparidari, A.; Dato, M. A.; Sterbinsky, G. E.; Wu, T.; Salehi-Khojin, A.; Pascal, T. A.; Cabana, J. Active States During the Reduction of CO_2 by a MoS_2 Electrocatalyst. *J. Phys. Chem. Lett* **2023**, *14*, 3222−3229.
(33) Zhu, Q.; Gu, Y.; Wang, X.; Gu, Y.; Ma, J. The Synergistic Effect between Metal and Sulfur Vacancy to Boost CO_2 Reduction Efficiency: A Study on Descriptor Transferability and Activity Prediction. *JACS Au* **2024**, *4*, 125−138.
(34) Pedretti, E.; Restuccia, P.; Righi, M. C. Xsorb: A Software for Identifying the Most Stable Adsorption Configuration and Energy of a Molecule on a Crystal Surface. *Comput. Phys. Commun* **2023**, *291*, 108827.
(35) Martí, C.; Blanck, S.; Staub, R.; Loehlé, S.; Michel, C.; Steinmann, S. N. DockOnSurf: A Python Code for the High-throughput Screening of Flexible Molecules Adsorbed on Surfaces. *J. Chem. Inf. Model* **2021**, *61*, 3386−3396.
(36) Larsen, A. H.; Mortensen, J. J.; Blomqvist, J.; Castelli, I. E.; Christensen, R.; Dułak, M.; Friis, J.; Groves, M. N.; Hammer, B.; Hargus, C.; et al. The Atomic Simulation Environment—A Python Library for Working with Atoms. *J. Phys.: condens. Matter* **2017**, *29*, 273002.
(37) Peterson, A. A.; Abild-Pedersen, F.; Studt, F.; Rossmeisl, J.; Nørskov, J. K. How Copper Catalyzes the Electroreduction of Carbon Dioxide Into Hydrocarbon Fuels. *Energy Environ. Sci* **2010**, *3*, 1311.
(38) Hohenberg, P.; Kohn, W. Inhomogeneous Electron Gas. *Phys. Rev* **1964**, *136*, B864−B871.
(39) Kohn, W.; Sham, L. J. Self-Consistent Equations Including Exchange and Correlation Effects. *Phys. Rev* **1965**, *140*, A1133−A1138.
(40) Perdew, J. P.; Burke, K.; Ernzerhof, M. Generalized Gradient Approximation Made Simple. *Phys. Rev. Lett* **1996**, *77*, 3865−3868.
(41) Kresse, G.; Hafner, J. *Ab initio* Molecular Dynamics for Open-shell Transition Metals. *Phys. Rev. B* **1993**, *48*, 13115−13118.
(42) Kresse, G.; Furthmüller, J. Efficient Iterative Schemes for *Ab initio* Total-energy Calculations Using a Plane-wave Basis set. *Phys. Rev. B* **1996**, *54*, 11169−11186.
(43) Blöchl, P. E. Projector Augmented-Wave Method. *Phys. Rev. B* **1994**, *50*, 17953−17979.
(44) Kresse, G.; Joubert, D. From Ultrasoft Pseudopotentials to the Projector Augmented-wave Method. *Phys. Rev. B* **1999**, *59*, 1758−1775.
(45) Grimme, S.; Antony, J.; Ehrlich, S.; Krieg, H. A Consistent and Accurate ab Initio Parametrization of Density Functional Dispersion Correction (DFT-D) for the 94 Elements H-Pu. *J. Chem. Phys* **2010**, *132*, 154104.
(46) Vlaisavljevich, B.; Huck, J.; Hulvey, Z.; Lee, K.; Mason, J. A.; Neaton, J. B.; Long, J. R.; Brown, C. M.; Alfè, D.; Michaelides, A.; Smit, B. Performance of van der Waals Corrected Functionals for Guest Adsorption in the M_2(dobdc) Metal−Organic Frameworks. *J. Phys. Chem. A* **2017**, *121*, 4139−4151.
(47) Freire, R. L. H.; Guedes-Sobrinho, D.; Kiejna, A.; Da Silva, J. L. F. Comparison of the Performance of van der Waals Dispersion Functionals in the Description of Water and Ethanol on Transition Metal Surfaces. *J. Phys. Chem. C* **2018**, *122*, 1577−1588.
(48) Nies, C.-L.; Nolan, M. DFT Calculations of the Structure and Stability of Copper Clusters on MoS_2. *Beilstein J. Nanotechnol* **2020**, *11*, 391−406.
(49) Han, J.; Fan, Y.; Yang, Y.; Liu, Z. Structural Evolution of MoS_2 Supported Gold Nanoclusters Under CO Oxidation Condition and the Effect on Reaction Activity. *Appl. Surf. Sci* **2021**, *543*, 148841.
(50) Press, W. H. Numerical Recipes. In *The Art of Scientific Computing*; Cambridge University Press, 2007.
(51) Reuter, K.; Scheffler, M. Composition, Structure, and Stability of RuO_2(110) as a Function of Oxygen Pressure. *Phys. Rev. B* **2001**, *65*, 035406.
(52) Cramer, C. J. The Potential Energy Diagram. In *Essential of Computational Chemistry: theories and Models*; John Wiley & Sons, Ltd, 2004; pp. 355−384.
(53) Nørskov, J. K.; Studt, F.; Abild-Pedersen, F.; Bligaard, T. The Potential Energy Diagram. In *Fundamental Concepts in Heterogeneous Catalysis*; John Wiley & Sons, Ltd, 2014, pp. 6−25. .
(54) Freire, R. L. H.; de Lima, F. C.; Fazzio, A. Vacancy Localization Effects on MX_2 Transition-metal Dichalcogenides: A Systematic Ab initio Study. *Phys. Rev. Mater* **2022**, *6*, 084002.
(55) Jackson, K. A. First-Principles Study of the Structural and Electronic Properties of Cu Clusters. *Phys. Rev. B* **1993**, *47*, 9715−9722.
(56) Chaves, A. S.; Piotrowski, M. J.; Da Silva, J. L. F. Evolution of the Structural, Energetic, and Electronic Properties of the 3*d*, 4*d*, and 5*d* Transition-metal Clusters (30 TM_n Systems for n = 2 - −15): A Density Functional Theory Investigation. *Phys. Chem. Chem. Phys* **2017**, *19*, 15484−15502.
(57) Puigdollers, A. R.; Schlexer, P.; Pacchioni, G. Gold and Silver Clusters on TiO_2 and ZrO_2 (101) Surfaces: Role of Dispersion Forces. *J. Phys. Chem. C* **2015**, *119*, 15381−15389.
(58) Kim, M.; Kim, W. J.; Lee, E. K.; Lebègue, S.; Kim, H. Recent Development of Atom-pairwise van der Waals Corrections for Density Functional Theory: From Molecules to Solids. *Int. J. Quantum Chem* **2016**, *116*, 598−607.
(59) Nørskov, J. K.; Bligaard, T.; Logadottir, A.; Kitchin, J. R.; Chen, J. G.; Pandelov, S.; Stimming, U. Trends in the Exchange Current for Hydrogen Evolution. *J. Electrochem. Soc* **2005**, *152*, J23.
(60) Marković, N. M.; Grgur, B. N.; Ross, P. N. Temperature-dependent Hydrogen Electrochemistry on Platinum Low-index Single-crystal Surfaces in Acid Solutions. *J. Phys. Chem. B* **1997**, *101*, 5405−5413.
(61) Skúlason, E.; Karlberg, G. S.; Rossmeisl, J.; Bligaard, T.; Greeley, J.; Jónsson, H.; Nørskov, J. K. Density Functional Theory Calculations for The Hydrogen Evolution Reaction in an Electrochemical Double Layer on the Pt(111) Electrode. *Phys. Chem. Chem. Phys* **2007**, *9*, 3241−3250.
(62) Ooka, H.; Huang, J.; Exner, K. S. The Sabatier Principle in Electrocatalysis: Basics, Limitations, and Extensions. *Front. Energy Res* **2021**, *9*, 654460.
(63) Da Silva, J. L. F. Effective Coordination Concept Applied for Phase Change $(GeTe)_m(Sb_2Te_3)_n$ Compounds. *J. Appl. Phys* **2011**, *109*, 023502.
(64) Li, J.; Ma, Y.; Ho, J. C.; Qu, Y. Hydrogen Spillover Phenomenon at the Interface of Metal-Supported Electrocatalysts for Hydrogen Evolution. *Acc. Chem. Res* **2024**, *57*, 895−904.
(65) Wang, Y.; Ding, J.; Deng, F.; Liu, H. Effect of Pt Clusters on Hydrogen Adsorption Behaviors of Cup-Stacked Carbon Nanotubes: A DFT Study. *Carbon Lett* **2024**, *34*, 1593−1608.
(66) Yeh, C.-H.; Thang, H. V.; Reyes, Y. I. A.; Coluccini, C.; Chen, H.-Y. T. DFT Insights into Hydrogen Spillover Mechanisms: Effects of Metal Species, Size, and Support. *J. Phys. Chem. C* **2025**, *129*, 6185−6195.
(67) Sihag, A.; Reyes, Y. I. A.; Lin, Y.-C.; Dyer, M. S.; Tiffany Chen, H.-Y. How Do Defects Affect Hydrogen Spillover on Graphene-Supported Pt? A DFT Study. *Mater. Today Sustainability* **2023**, *24*, 100554.
(68) Du, J.; Cai, T.; Han, Q.; Wu, H.; Zhao, Q.; Zheng, L.; Liu, S.; Yang, Z. Defect-Driven Hydrogen Evolution: Enhanced Hydrogen

Spillover on Pt-MoS_2 Interface via Sulfur Vacancies. *J. Colloid Interface Sci* **2025**, *692*, 137470.
(69) Li, M.; Yin, W.; Pan, J.; Zhu, Y.; Sun, N.; Zhang, X.; Wan, Y.; Luo, Z.; Yi, L.; Wang, L. Hydrogen Spillover as a Promising Strategy for Boosting Heterogeneous Catalysis and Hydrogen Storage. *Chem. Eng. J* **2023**, *471*, 144691.
(70) Shen, H.; Li, H.; Yang, Z.; Li, C. Magic of Hydrogen Spillover: Understanding and Application. *Green Energy Environ* **2022**, *7*, 1161−1198.
(71) Gaur, A.; Sharma, J.; Han, H. Hydrogen Spillover Effect in Electrocatalysis: Delving into the Mysteries of the Atomic Migration. *Energy Environ. Mater* **2024**, *7*, No. e12761.
(72) Shi, Y.; Zhang, S.; Liu, X.; Wang, S.; Gao, B.; Wang, J. Recent Advances in Hydrogen Spillover and Reverse Hydrogen Spillover for the Two-Dimensional Materials. *Mater. Today Sustainability* **2025**, *31*, 101194.
(73) Liu, Y.; Guan, S.; Du, X.; Chen, Y.; Yang, Y.; Chen, K.; Zheng, Z.; Wang, X.; Shen, X.; Hu, C.; Li, X. S-Vacancy Defect and Transition-metal Atom Doping to Trigger Hydrogen Evolution of Two-dimensional MoS_2. *Energy Fuels* **2023**, *37*, 5370−5377.
(74) van Deelen, T. W.; Hernández Mejía, C.; de Jong, K. P. Control of Metal-Support Interactions in Heterogeneous Catalysts to Enhance Activity and Selectivity. *Nat. Catal* **2019**, *2*, 955−970.
(75) Smiljanić, M.; Panić, S.; Bele, M.; Ruiz-Zepeda, F.; Pavko, L.; Gašparič, L.; Kokalj, A.; Gaberšček, M.; Hodnik, N. Improving the HER Activity and Stability of Pt Nanoparticles by Titanium Oxynitride Support. *ACS Catal* **2022**, *12*, 13021−13033.
(76) Teng, X.; Si, D.; Chen, L.; Shi, J. Synergetic Catalytic Effects by Strong Metal−Support Interaction for Efficient Electrocatalysis. *eScience* **2024**, *4*, 100272.
(77) Man, I. C.; Su, H.-Y.; Calle-Vallejo, F.; Hansen, H. A.; Martínez, J. I.; Inoglu, N. G.; Kitchin, J.; Jaramillo, T. F.; Nørskov, J. K.; Rossmeisl, J. Universality in Oxygen Evolution Electrocatalysis on Oxide Surfaces. *ChemCatchem* **2011**, *3*, 1159−1165.
(78) Wang, G.; Jiang, X.-L.; Jiang, Y.-F.; Wang, Y.-G.; Li, J. Screened Fe_3 and Ru_3 Single-cluster Catalysts Anchored on MoS_2 Supports for Selective Hydrogenation of CO_2. *ACS Catal* **2023**, *13*, 8413−8422.

https://doi.org/10.1021/acscatal.5c05963
ACS Catal. 2025, 15, 20036−20048